

Prediction of Frangible Joint Dynamic Fracture and Shock Output Characteristics

Joshua E. Gorfain¹

Quartus Engineering, Inc., Herndon, VA, 20171, USA

Frangible joints provide controlled separation of continuous structural connections on aerospace systems such as launch vehicles, rockets, and spacecraft. These devices are critical to mission success as they enable inter-stage separation and payload delivery. Severance of the joint is governed by an explosive-induced impulsive loading that drives dynamic fracture of a structural member. The prediction of frangible joint performance was studied, in terms of shock output and severance, using nonlinear dynamic finite element analysis. Physics-based simulation of fundamental device behavior was validated relative to open-source experimental data. Sensitivities of device separation performance and shock output to joint structural material properties were subsequently explored to better understand these complex devices. Insights towards better performing, lower shock frangible joint designs are discussed.

I. Introduction

Many launch vehicles and rockets in service today utilize frangible joints to facilitate separation of vehicle stages during launch. Payload deployment may also be accomplished by frangible joint (FJ) devices where continuous structural joints are employed. Proper device functionality consists of complete severance once the activation command is given. Frangible joint performance is therefore critical to mission success. Understanding the complex behavior of successful FJ severance could reduce the risk of inadvertent failure, defined as incomplete separation. Investigating the mechanics of device functional performance through computational analysis could provide useful information into the conditions under which successful severance does or does not occur. This in turn would help to achieve more robust and reliable device designs and improve reliability where these systems are fielded. Continued occurrence of mission failures attributed to frangible joint malfunction suggests that further study and improvements are needed. For example, the crash of the NASA Orbiting Carbon Observatory satellite in 2009 was in part attributed to failure of a frangible joint subsystem that did not properly separate a stage [1]. A similar failure led to the loss of the Glory climate monitoring spacecraft in 2011 [2]. The difficulty and persistence of this problem is exemplified by a more recent failure; the attempted launch of the classified Zuma satellite in the 2018 that resulted in a total loss [3].

A secondary concern associated with frangible joints is the shock loading produced as a by-product of its function. Frangible joints use explosives (pyrotechnics) to provide rapid and reliable actuation. Once commanded, explosive detonation-induced shock loads are transmitted through attached structure. Resulting dynamic environments are referred to as pyroshock, distinct from other types of shock events. Pyroshock environments can readily cause avionics and other sensitive systems to malfunction or fail, potentially leading to a different type of mission failure. This risk often drives the requirements for equipment survivability and qualification.

Successful FJ operation is the controlled and reliable severance of the joint, achieved mechanically. The severance process for a generic frangible joint is illustrated schematically in the sectional views of Fig. 1, taken from Duprey and Keon [4]. This sequence occurs from left-to-right, where the nominal joint state is shown in the left-most image, marked as state 1. The FJ assembly consists of a structural section commonly made of an aerospace-grade aluminum extrusion, providing a central cavity as shown. Designs may alternatively use several parts joined mechanically rather than the single structural element shown. Within the joint cavity is an expanding tube assembly (XTA), consisting of an explosive filled mild detonating fuse (MDF), an elastomeric charge holder, and a steel confinement tube. The activation command detonates the MDF explosive (state 2), where energy release in the form of high-pressure detonation products causes the confinement tube to rapidly expand (state 3). This tube expansion imparts a lateral loading to the sides of the joint structural member within which it is contained, such that fracture occurs in the notched

¹ Engineering Manager, Aerospace Sector, and AIAA Member.

region (state 4). This sequence occurs on a time scale on the order of 10s of microseconds and is highly dynamic in nature. Note that in a stage separation arrangement, the joint cross-section geometry shown in Fig. 1 is revolved about the rocket cylindrical axis, located at a radial distance from the centerline of the joint section. Thus, a large ring-shaped frangible joint assembly would attach adjacent rocket sections axially using additional bolted connections (not shown here). Therefore, during operation, the FJ would unzip as the detonation wave runs along the circumferential path of the MDF.

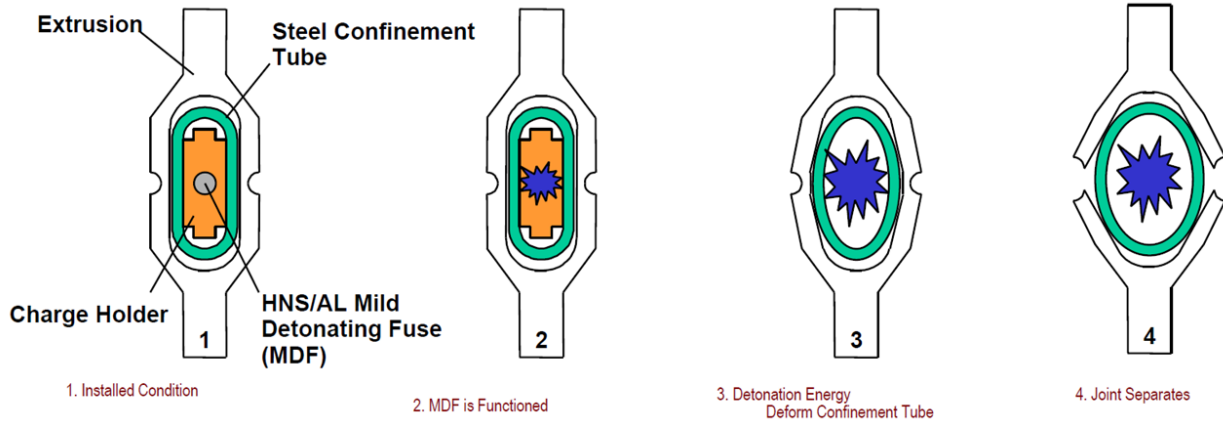


Fig. 1 Cross-sectional schematic of generic frangible joint operation, from Duprey and Keon 2006 [4]; reprinted by permission of the American Institute of Aeronautics and Astronautics, Inc.

The criticality of frangible joint performance has led to a number of investigations on this topic in the literature. Alcantara [5] studied the metallurgical and fractographic characteristics of the FJ structural member through quasi-static experiments. This work focused on identifying key design features contributing to the stress state and ultimate fracture process. A static test method was devised to avoid the complexity of the dynamic loading and response observed in flight-like systems, leading to a simplified laboratory approach to design screening and qualification/acceptance activities. Tests performed also aimed to correlate various member design variables to performance, i.e. severance. But these static experiments failed to capture the true dynamics of loading during device function that is intimately related to joint fracture and shock output. Choi et al. [6] developed computational models of a linear-explosive-filled expanding tube (i.e. an XTA) that were used to simulate the variation in tube expansion as a function of core load (the amount of explosive fill used). Experimental measurements were also performed to provide data for use in evaluating model accuracy. This work focused solely on the load-producing component of a frangible joint. Beyond exploring the conditions under which the confining tube might fail to contain the detonation products, implications on actual FJ device performance were not studied.

Computational modeling of other types of aerospace ordnance devices has been performed previously. Through modeling using the Autodyn-2D code, Chambers [7] designed a linear shaped charge (LSC) separation system for the Ares I rocket. This work employed constitutive modeling designed to represent the shaped charge jet penetration mechanism unique to the LSC. Goldstein et al. [8] evaluated the performance of a satellite separation system bolt cutter device. Simulations using the MESA-2D and DYNA3D computational codes explored device characteristics on cutter performance. Wang et al. [9] presented a similar, more contemporary effort focused on a separation nut. Induced shock environments resulting from separation nut firing were also explored. While all insightful works, these efforts did not address the FJ device that is more commonly used in modern applications, when sensitive systems or shock environment concerns are involved.

Frangible joint modeling has been demonstrated within a design context by device designers such as [4] and Duprey and Saucier [10]. These works did not present detailed information regarding the development of computational models or the physics of their operation but were instead more focused on the basic demonstration of concept success. Ott and Folkman [11] documented modern pyroshock shock environment data from full-scale testing of a cylindrical structure separated by a LSC device. This work was focused entirely on the shock environment produced by operation of the LSC rather than the detailed physics of the device itself. It demonstrated a clear need for an improved understanding of ordnance device-induced shock environments. Connecting device physics to shock output is a logical step towards fulfilling this need. Mission success relies on the survival of equipment and systems under pyroshock environments encountered during flight. Survivability is typically demonstrated through laboratory-

based pyroshock testing as part of launch certification. McLeod and Tatum [12] described numerical simulations of this type of pyroshock simulation testing, intended to supplement and guide experimental activities from a test laboratory view. Explicit simulation of the explosive detonation, wave propagation, and subsequent shock environment was performed. This application was narrowly focused on qualification activities using an ordnance surrogate rather than a flight-like device. Verification of pyroshock survival would benefit from the work by McLeod and Tatum but no connection is made to FJ performance or incomplete separation.

The work documented herein was focused on simulating the detailed physical mechanisms of complete FJ operation, supported by available open-source experimental data. To this end, appropriate computational constitutive models for all materials of the device were developed using data from the literature. This included the explosive, multiple types of metals, and an elastomer. Once predictive credibility was established, the model was perturbed to explore the sensitivity of FJ performance to structural material selection. Insights gained from this work sought to inform better FJ designs as they relate to improved launch reliability.

II. Computational Modeling

A two-part modeling effort was carried out to validate simulations of key phenomena associated with frangible joint operation. First, static experiments by Alcantara [5] were simulated to validate the mechanics and fracture initiation process of the FJ structural member alone. A complete frangible joint model was then constructed to simulate the dynamic fracture event essential to its functional performance. The fidelity of this FJ model was validated relative to experimental results from Duprey and Keon [4]. With confidence in the modeling established, FJ performance was studied by varying structural material selections to predict potential effects on device functional performance and shock output.

A full-scale frangible joint employed on a rocket is a large cylindrical component. The axisymmetric nature of the joint relative to the launch vehicle cylindrical axis allows for a two-dimensional model to be used for computational efficiency. A two-dimensional plane strain model of the joint cross-section was adopted for this numerical problem. This modeling approach was sufficient for this investigation as FJ operation is a quasi-2D process as the joint unzips circumferentially. While technically axisymmetric, the large difference in length scale among the FJ section and the launch vehicle or rocket diameter of the full joint ring assembly permits the plane strain approximation. Similar reduced scale modeling has been utilized in the literature with plane strain-type behavior seen experimentally [4-5], thus demonstrating the validity of this model simplification. Initial studies found no discernable difference among results from plane strain and axisymmetric simulations at the length scales explored here. Because of this and the idealized tolerance condition of the assembly, half-symmetric models of the FJ cross-section were used to achieve further gains in computational efficiency.

The Abaqus finite element code [13] was used for all simulations. The Standard (implicit) solver was employed for solution of the nonlinear elastoplastic boundary value problem of static joint fracture experiments. Functional performance of the complete frangible joint was simulated using the explicit dynamics hydrocode solver, employing the coupled Eulerian-Lagrangian (CEL) computational technique. Explicit time integration is best suited to the very high strain rates associated with the explosive loading, as well as the nonlinear mechanics and dynamic fracture processes. The energy equation was solved under the adiabatic assumption as heat transfer processes would occur over much longer timescales than the rapid heating from mechanical and hydrodynamic deformations of this high-rate event. A Eulerian spatial discretization was used to solve for the extreme deformation and flow anticipated for materials within the expanding tube (detonation products, inert MDF and charge holder materials). Treating these components with a Lagrangian discretization would likely fail due excessive mesh distortion. Lagrangian finite elements were used to discretize the expanding tube as its deformation is more modest in comparison, despite the significant plastic deformations it is expected to undergo. These separate Eulerian and Lagrangian domains communicated through a coupling algorithm based on an enhanced immersed boundary method, enforced using a penalty method. For the assembled frangible joint (frangible structural member and XTA), an additional contact algorithm enabled interaction of the various mechanical components. Subsequent pyroshock environment predictions utilized the novel technique from Gorfain [14] for predicting FJ-induced pyroshock environments. This entailed deriving the shock excitation from FJ simulations and mapping this load (spatially and temporally varying forcing functions) to a structural model of a generic test plate. Subsequent explicit dynamics simulations were then conducted to predict the transient shock response of the plate induced by functioning the FJ attached along one of its edges.

A. Static Fracture

Static fracture testing conducted by Alcantara [5] utilized a simplified joint test specimen consisting of a half symmetric portion of the frangible member (clevis) cross-section. This was done to provide access for the loading ram

to contact the inside of the clevis side so as to load the joint structural element laterally, in a manner comparable to that of the XTA in the full FJ assembly. Details regarding the dimensions of this static joint specimen derived from [5], consistent with [4,10], Stockinger et al. [15], and Fritz [16]. This nominal FJ clevis structural detail included the vital frangible feature, the notch and ligament region, as shown in Fig. 2. The remote portions of the joint member away from the notch was not expected to substantially contribute to fracture in the notch region, and so was constrained in the model to match the clamped grips used in the tests.

The static test specimen was modeled with linear-interpolation, reduced-integration, three-dimensional hexahedral finite elements. A very refined mesh size of 50 μm was defined to adequately resolve field variables and fracture within the frangible region: the notch, inside fillet, and ligament. Smooth transitions to a larger mesh size were used elsewhere where such a high level of refinement was not necessary. Fixturing used in the test was approximated as fixed (zero displacement) boundary conditions to surfaces within the grip regions. Load application was idealized as an applied pressure over the load ram engagement area. The left image in Fig. 2 illustrates the static test configuration modeled.

A key aspect of this analysis is material constitutive modeling, where plasticity and fracture descriptions for the frangible material are crucial. The widely used Johnson-Cook strength [17] and fracture [18] models were used for this purpose. The strength model employs a phenomenological description of the variation in flow stress due the effect of strain hardening, rate-sensitivity, and thermal softening associated with adiabatic heating. The flow stress is given by,

$$Y = [A + B(\bar{\epsilon}^p)^n][1 + C \ln \dot{\epsilon}^*][1 - T^{*m}], \quad (1)$$

where $\bar{\epsilon}^p$ is the equivalent plastic strain, $\dot{\epsilon}^* = \dot{\bar{\epsilon}}^p / \dot{\epsilon}_0$ is the dimensionless plastic strain rate with $\dot{\epsilon}_0$ being a reference value (typically taken as 1 s^{-1}). The variable $T^* = (T - T_r) / (T_m - T_r)$ is the homologous temperature that is a function of the current material temperature T , a reference temperature T_r (typically room temperature), and the melting temperature T_m . The parameter A is the initial yield strength while B and n define strain hardening. Parameter C defines strain-rate sensitivity while m controls thermal softening. Isotropic plasticity using J2 flow theory is used to compute the accumulation of plastic strain given the Eq. (1) yield function.

The Johnson-Cook fracture model is capable of predicting the arbitrary initiation and growth of ductile fracture when combined with element erosion. This approach to fracture modeling was chosen here based on the success of its use documented throughout the literature: see for example Corona and Orient [19], Kay [20], and Senthil et al. [21]. One particular advantage in this approach is that a pre-defined crack path is not required, in contrast with cohesive element approaches. The fracture model is centered on damage growth and a phenomenological description of the equivalent plastic failure strain given by,

$$\bar{\epsilon}_f^p = [D_1 + D_2 \exp(-D_3 \sigma^*)][1 + D_4 \ln \dot{\epsilon}^*][1 - D_5 T^*]. \quad (2)$$

The form of Eq. (2) is intended to account for the sensitivity of ductile fracture to stress state through a dependence on the triaxality, $\sigma^* = -P/\bar{\sigma}$, with pressure $P > 0$ for compression and the von Mises equivalent stress $\bar{\sigma}$. The parameter D_1 is the nominal failure strain while D_2 and D_3 control the stress-state dependence. Parameters D_4 and D_5 control strain-rate and temperature dependencies, respectively. This fracture model utilizes an incremental damage parameter (D) defined as the ratio of current plastic strain increment to the current value of failure strain computed from Eq. (2). Damage accumulates by integrating the damage parameter in time, throughout the loading history. When this monotonically increasing damage parameter reaches a value of unity in a given finite element, failure (fracture) is indicated. Accordingly, the model was set to instantaneously degrade the material strength to zero and delete the corresponding element. This choice leads to the immediate loss of load carrying capacity at failure within an element, consistent with prompt fracture. Deletion of elements is the numerical approximation of free surface creation upon fracture employed in this work. It is acknowledged that the resulting stress-softening behavior and element erosion technique leads to mesh dependence. Exploration of provisions to potentially mitigate this mesh sensitivity were not pursued here given the good results obtained, as discussed later.

The specimen used by Alcantara was fabricated from 7075-T7351 aluminum alloy, which was also indicated in at least one other specific frangible joint design [4]. Adequate material information to support the constitutive model for this specific alloy treatment was not found in the open literature. Therefore, information provided in Brar et al. [22] for a comparable aluminum alloy, 7075-T651, was used here. Additionally, required elastic and thermophysical material properties were taken from Steinberg [23] and Rice et al. [24].

In the experiments, the load was increased until the onset failure was observed from digital image correlation (DIC) diagnostics and load-displacement data. The static simulation was conducted similarly, with the intent being to demonstrate reasonable prediction of the onset of fracture, associated with the local stress fields in way of the notch region while under load well-defined loads. Crack initiation in the simulation occurred at the instant when the fracture model damage parameter reached a value unity within any elements in the model. Representative simulation results for the local strain field included in Fig. 2 shows the expected stress concentration effects within the notch ligament region.

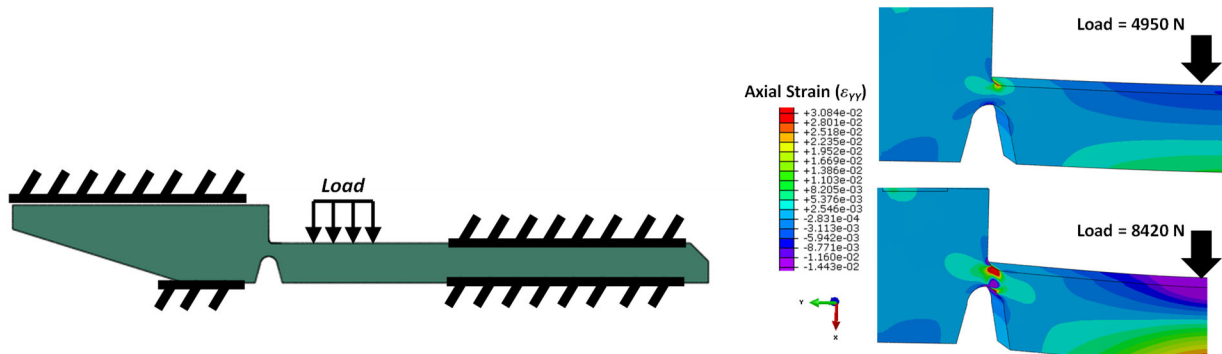


Fig. 2 Schematic of joint structure lateral test configuration in [5] and representative strain fields predicted here under different static load levels before fracture.

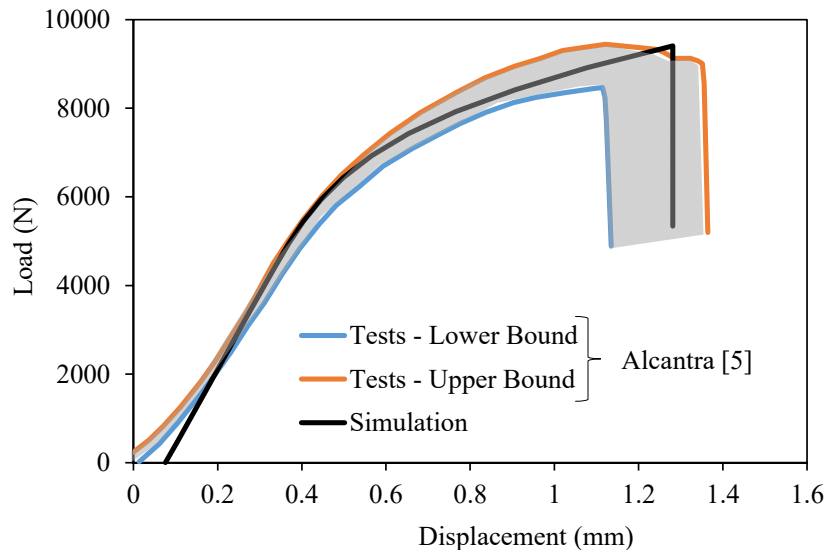


Fig. 3 Comparison of measured and predicted joint lateral load-displacement response.

The predicted load-displacement curve at the point of load application is overlaid with enveloped experimental data from [5] in Fig. 3. Initially ramped portions of the measured curves are consistent with slippage and closure of slack in the load train as the specimen becomes seated under the load ram. The linear portion of the curves was taken as the true specimen response once fully seated, and so the simulation result (which did not include slip) was shifted slightly to align with this linear portion. Excellent agreement is seen among the measured and predicted curves for the entire load range once seating was reached. The apparent softening under increasing load and ultimate load capacity was captured quite well. The fracture point in the simulation corresponded to the drop in the curve at a load of approximately 9400 N and 1.25 mm displacement. This prediction matches the average failure point (load and displacement) seen in the tests quite well, thus demonstrating adequate confidence in frangible structural modeling.

B. Dynamic Fracture

A computational model of the full FJ assembly was generated. The XTA was first constructed from information provided in Choi et al. [6]. The MDF consisted of an aluminum sheathed HNS explosive core, consistent with known frangible joint designs described in [4,10,16] and Bement and Schimmel [25]. A nominal HNS core load of 0.21 g/m (22 gr/ft) was modeled as it is within the typical range for these devices [4,6]. The elastomeric MDF holder and 304 stainless steel expanding tube was defined according to [6]. The plane-strain CEL model of the XTA is shown in Fig. 4. Figure Fig. 4a) shows the full Eulerian computational grid, where a relatively fine mesh was defined to encompass nearly the entire region of expected expansion. This grid sizing was set to maintain a minimum of 10 cells through the thickness of any material. All of the gray regions seen in Fig. 4a) corresponded to initial void volume in this background grid. The Lagrangian finite element mesh of the tube and initial geometries of the Eulerian material components (void hidden for clarity) are shown in Fig. 4b).

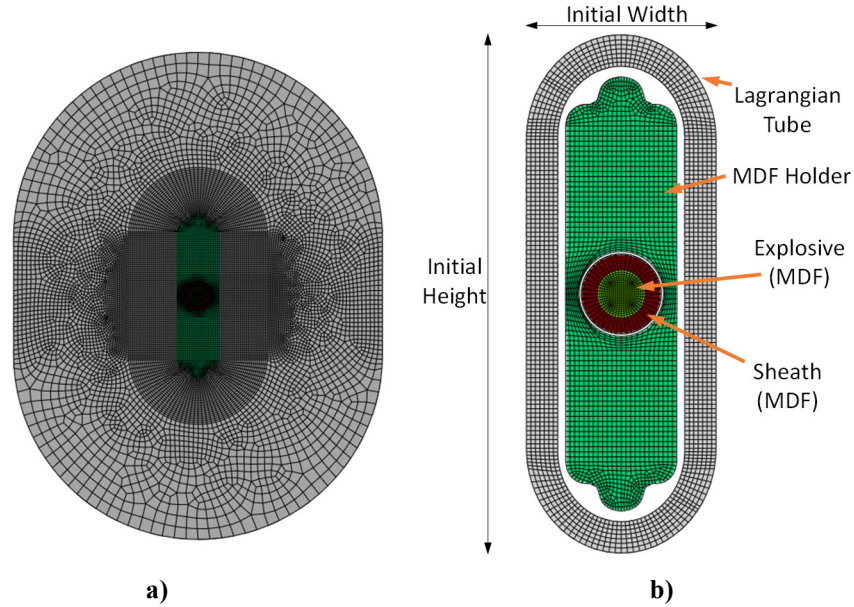


Fig. 4 Expanding tube assembly model, a) complete Eulerian domain, and b) material definitions.

Modeling the complexities of the XTA materials under the explosive loading requires particular attention. The HNS explosive core material was modeled using the JWL equation of state (EOS) following Lee et al. [23]. The JWL EOS describes the thermodynamic pressure-volume-energy states of explosive detonation products. Detonation of the explosive was computed analytically based on wave arrival timing for the geometry given the known, steady detonation velocity of the explosive. This is also known as the programmed burn algorithm. It was assumed that the MDF sheath was made of 6061-T6 aluminum consistent with [6]. The close proximity of the sheath with the explosive detonation products suggested it will be loaded to large compression by relatively strong shock waves. Therefore, a Mie-Gruneisen EOS [13] was used to describe this material, along with the Johnson-Cook strength model. The Mie-Gruneisen form used assumes the principal Hugoniot (the locus of thermodynamic states that can exist behind a shockwave propagating in an initially undisturbed material) can be represented by a linear relationship between shock velocity, U_S , and particle velocity, u_p . This leads to a pressure relation that is a linear combination of mechanical and thermal-energy terms. Expectations of sheath fragmentation led to a treatment using the Johnson-Cook failure model. The large compressions expected for the elastomer MDF holder necessitated an EOS description of its nonlinear volumetric response. A linear $U_S - u_p$ relation was considered inadequate to characterize the nonlinearities exhibited by this elastomer. Steinberg [23] gives a Mie-Gruneisen form that instead assumes a nonlinear $U_S - u_p$ relation and more general-purpose EOS form. The elastomer is very low strength compared to the metals with which it interacts, so a simple constant flow stress strength model was employed. This was chosen for its relevance to the high-rate, short duration shock loading during XTA operation where potential viscoelastic effects were not expected to be particularly important. The stainless-steel tube would undergo large deformations as it changes shape during expansion, but it does not break (per design intent). Accordingly, the Johnson-Cook strength model was used to describe the flow stress of the tube without the need for a failure model.

All material model parameters were taken from well documented, open literature sources. Parameters for the JWL EOS of HNS were taken from [26] for an initial density consistent with the nominal core loading described above. The Mie-Gruneisen parameters for the 6061-T6 sheath were taken from Steinberg [23] while Johnson-Cook strength and failure parameters were obtained from Lesuer et al. [27]. The specific type of elastomer used in the MDF holder was not well documented. A compilation of data from a variety of sources was used to populate a complete set of constitutive parameters as a single data source was not found. Parameters for the Steinberg form of the Mie-Gruneisen EOS for a silastic are contained in [23]. The shear wave speed of a silastomer (Sylgard) in Millett et al. [28] was used to estimate its shear modulus. The elastomer is very low strength compared to the metals with which it interacts, so this material was treated using a simple constant flow stress strength model. The dependence of shear strength on shock stress for Sylgard in [28] was used to assume a nominal value for the constant flow stress model. A value for specific heat was taken from Coe [29]. Properties for the 304 stainless steel tube were taken from [23] and Maurel-Pantel et al. [30].

The XTA model was integrated with joint structural components, resulting in the complete FJ computational model shown in Fig. 5. The left image of Fig. 5 shows the full FJ finite element mesh while the right image shows a close-up view of the notch region and XTA. Eulerian materials internal to the XTA are shown colored by initial density. The structural portion of the FJ consists of the frangible member (clevis) and the lower joint component (tang). These two components are attached through a bolted connection as indicated in Fig. 5, modeled simply as a tied (fully bonded) constraint at the effective connection regions shown. This simplification adequately reflects the mechanics of this joint connection within the context of this plane strain model. While not shown, these structural parts would extend above and below the joint region as they interface with larger scale systems, such as different stages or the rocket of fairing. The separation plane is thus defined by the notch position. Activation of the FJ detonates the MDC, which induces stress waves that propagate outwards from the XTA and transmit through all structural load paths. Simulation of FJ functional performance was performed for an analysis duration of 75 μ s. This was a sufficient duration for complete severance to occur and reach a deformed FJ geometry in a near-equilibrium state.

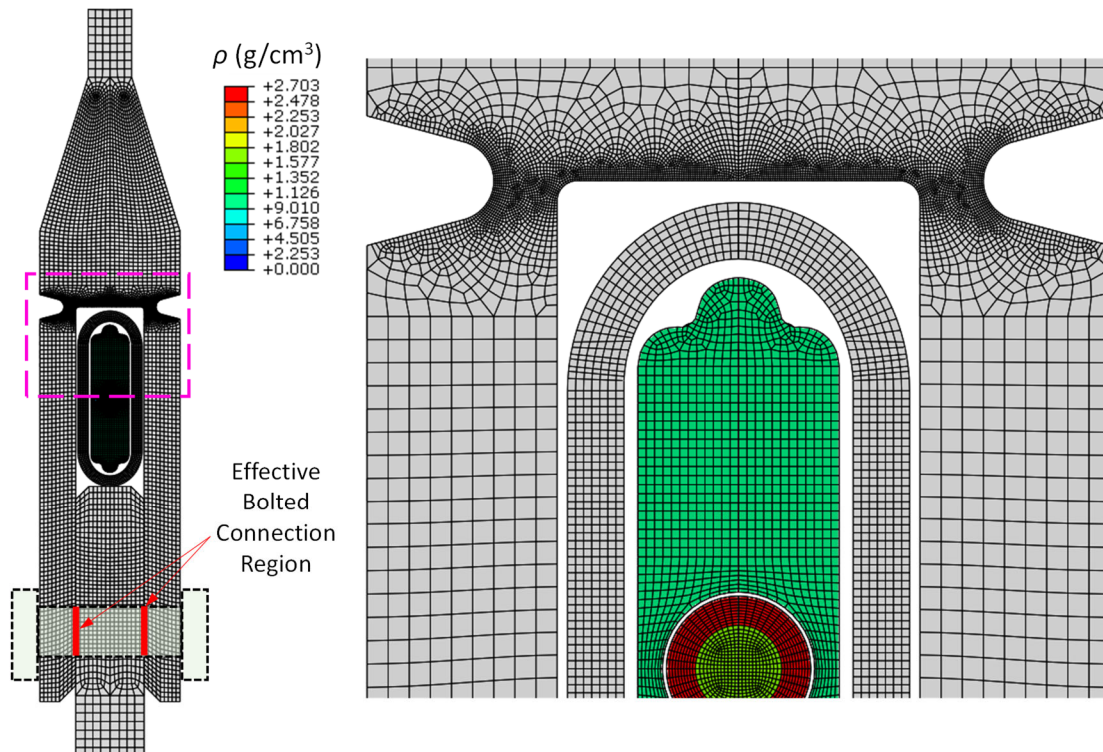


Fig. 5. Frangible joint computational model.

Duprey and Keon [4] provided some photographs of FJ condition following functional performance testing using a configuration that is essentially the same as this model. Imagery documented post-separation deformation of the FJ structure below the separation plane (notch) and was used as an experimental reference for model validation. Photographs are available for two unspecified core loads, simply designated as 80% and 120% conditions ($\pm 20\%$

nominal). These post-test photographs are shown in Fig. 6 with the corresponding FJ simulation result for the assumed nominal core load, shown at approximately the same scale and view. Outward (flaring) deformations and basic fracture regions are the primary observables in the photographs. The simulation result matched these experimental images quite well, especially when considering the variability in core load involved.

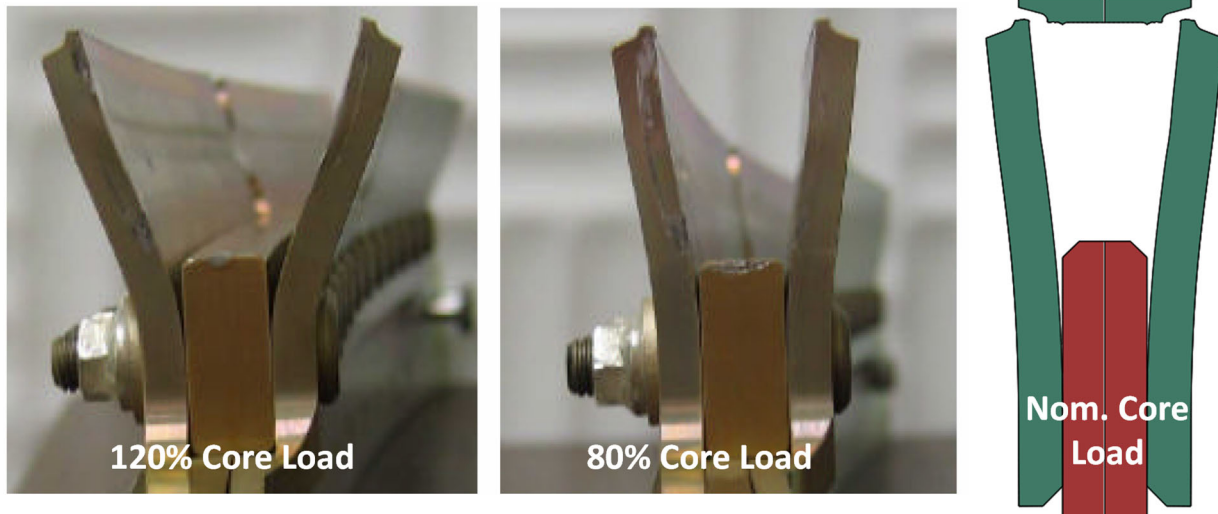


Fig. 6 Comparison of post-separation FJ deformed state, simulation (right) and experimental results from [4]; reprinted by permission of the American Institute of Aeronautics and Astronautics, Inc.

The complete sequence of FJ functional behavior predicted by the model is shown in Fig. 7. It was seen to take roughly $13 \mu\text{s}$ for the XTA-induced loading to initiate a crack at the inside fillet region of the FJ. The inside fillet radius is smaller than the notch root (by a factor of 2) and so was the location of the sharpest stress concentration. Outward bending of the joint sides produced primarily tensile stresses at the inside fillet, more likely to initiate a crack than the predominantly compressive stress at the notch root. Both of these considerations explain the calculated initiation site. Continued lateral loading by XTA expansion drove fracture propagation such that complete severance was seen by approximately $25 \mu\text{s}$ after detonation. This timing resulted in a nominal crack propagation speed of $\sim 0.07 \text{ mm}/\mu\text{s}$ that is roughly two orders of magnitude slower than the $\sim 2.8 \text{ mm}/\mu\text{s}$ Rayleigh wave speed that is the limiting crack propagation velocity for this aluminum alloy. Such a large disparity in time scale suggests the observed dynamic fracture is more consistent with a mechanically driven mechanism than being strongly driven by wave propagation alone.

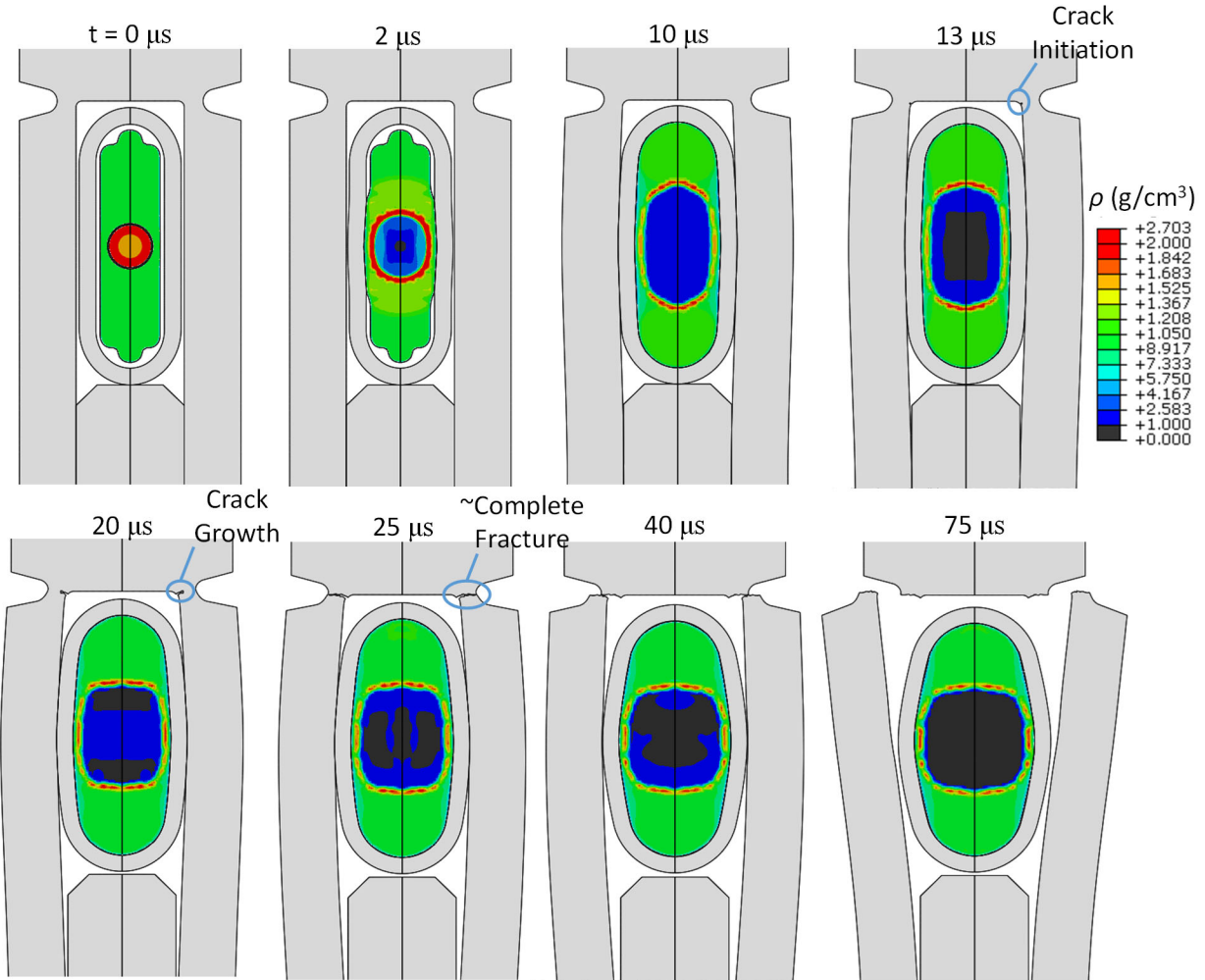


Fig. 7 Computed FJ function and dynamic fracture progression for 7075-T651 aluminum joint structure.

A more in-depth look at the mode of fracture is considered in Fig. 8 by viewing contours of triaxiality computed throughout the fracture sequence. Recall that triaxiality $\sigma^* > 0$ indicates a tensile stress state while $\sigma^* < 0$ indicates compression. Predominantly shear states are indicated by $\sigma^* \approx 0$, uniaxial stress tension and compression correspond to $\sigma^* = \pm 1/3$, and states of pure hydrostatic stress are $\sigma^* \gg \pm 2$. Prior to crack initiation (12 μs), the inside fillet is seen to be in a state of roughly equal parts hydrostatic tension and shear that corresponds to a relatively low failure strain for this material. Elevated stresses and a low threshold for failure renders this a reliable fracture initiation site, by design. In contrast, much of the ligament is in a state of primarily shear (with low levels of hydrostatic tension) that transitions to a combined stress state with elevated hydrostatic compression at the notch root.

The initiated $\sim 45^\circ$ angled crack seen at 13 μs is consistent with mode I (tensile) fracture given the geometry and stress state of the inside fillet. Subsequent crack growth briefly continues along the $\sim 45^\circ$ path until roughly 15 μs , after which time the path appears to instead travel horizontally (along 0°). The stresses ahead of the propagating crack appear to remain in a relatively consistent state of shear dominated tension. Locating the notch at the top of the joint as with the geometry modeled here, results in fracture dominated by shear failure according to Fritz [16]. In contrast, a more centrally located notch as in Fig. 1 would lead to failure in primarily tension. Shear loading is preferred over pure tension as lower energy input is needed to drive failure. Lower energy demand tends to translate into more reliable and efficient joint severance, translating to greater margin for successful separation. The tensile initiated, shear driven fracture process shown in Fig. 8 is consistent with FJ design intent and the experimentally observed severance mechanism described in [16], providing credibility to the simulation. It is recognized that a more refined mesh or alternative mesh pattern might have resulted in smoother crack surfaces and increased surface rubbing that may be expected in practice. Even so, the principal fracture processes predicted are expected to remain unchanged.

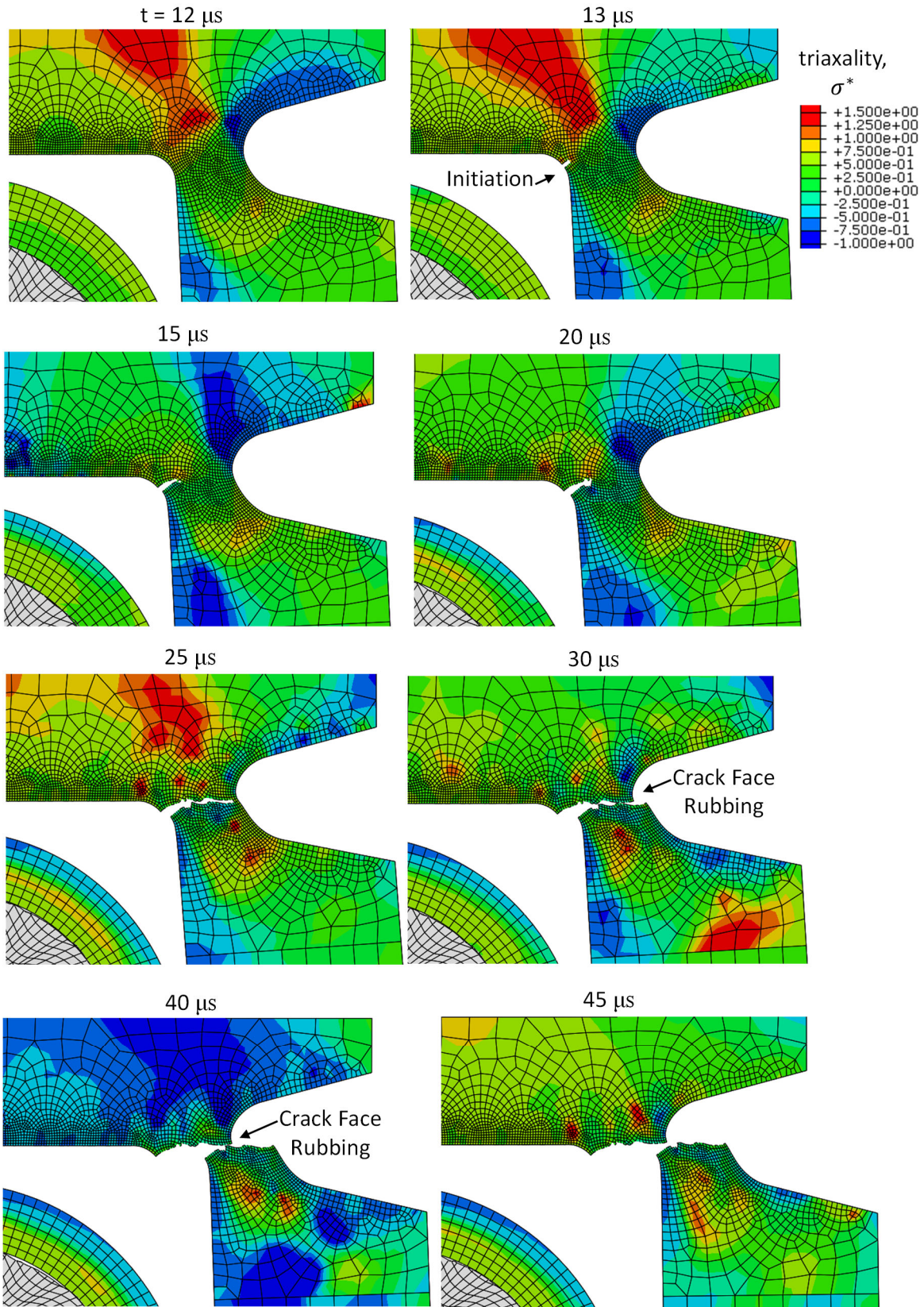


Fig. 8 Computed notch-ligament stress states (triaxiality) during fracture.

C. Fracture Performance Study

Having established a credible FJ computational model that demonstrated the primary mechanisms of its operation, additional performance characteristics and sensitivities were explored. The effect of alternative frangible structural material alloys on FJ performance is of particular interest. Severance is primarily governed by the strength and fracture behavior of the frangible material, with the structural geometry (notch-ligament) and XTA sized accordingly. Simulating FJ performance for a variety of frangible structural material choices can provide insight into the robustness of the design and how performance characteristics may be altered, either positively or negatively. Another performance characteristic of particular interest is the effect on shock output, ultimately in terms of transmitted pyroshock environments of attached structures and systems.

Studies here varied the material employed for the FJ structural components while leaving the XTA and all other features unchanged, and so specifically isolating the material effect on predicted performance. The FJ structure should be made of a high-strength aerospace grade alloy to meet the various performance requirements imposed on such an integral part of the launch vehicle or rocket system. As such, two alternative joint materials were considered relative to the baseline 7075-T651 aluminum alloy; a similar 7075-T6 alloy, and a high strength titanium alloy, Ti6Al4V. Constitutive equations of the frangible joint structural material were not changed. Model parameters employed were simply edited to reflect the behavior specific to the alternative alloys studied. Thermophysical, strength, and failure model parameters for the 7075-T6 alloy were provided in [22]. Material parameters for Ti6Al4V were obtained from [23, 27].

Specific comparison of the viscoplastic characteristics for each material was made through examining their adiabatic responses under uniaxial stress tension, at a strain rate of $3 \cdot 10^4 \text{ s}^{-1}$. While this simple loading condition is a crude approximation of the true multiaxial state occurring in the FJ notch ligament, it does provide a relevant and straightforward basis for comparison. The strain rate chosen corresponds to the nominal value computed in the ligament during the baseline separation simulation. Flow stress-equivalent plastic strain curves were computed to failure (as indicated by the fracture model), these are shown Fig. 9 as heavy solid lines. Dashed lines denote the corresponding dissipated strain energy associated with plastic work. The 7075-T6 alloy is seen to exhibit greater dissipated strain energy than the 7075-T651, due to greater overall strength given similarities among hardening and strain at fracture. In contrast, the much greater strength of the titanium comes at the expense of a much lower strain at fracture, and so only about half as much energy is dissipated before failure. This is a fundamental characteristic of the less ductile titanium as compared to the aluminum alloys.

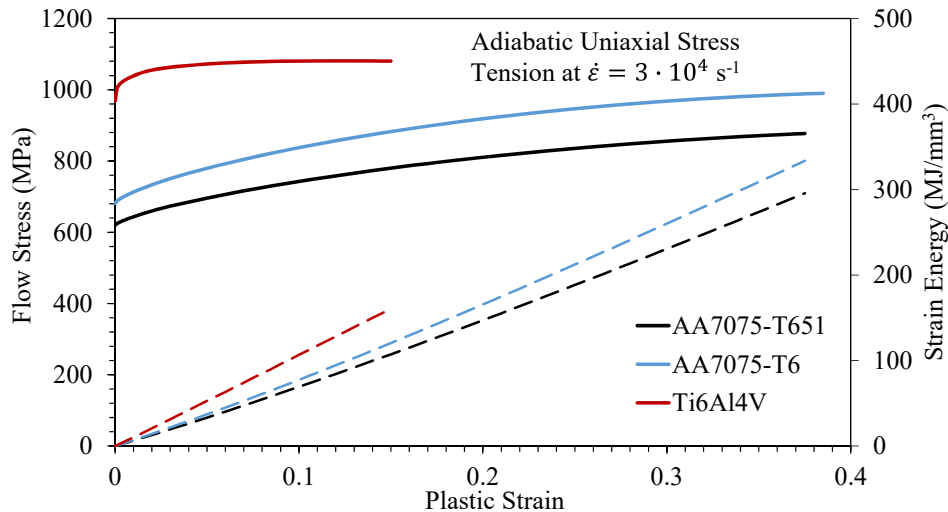


Fig. 9 Computed high-rate uniaxial stress tension responses among frangible structural materials considered.

The net effect of the different structural materials on FJ functionality is first illustrated through the near-equilibrium post-function deformed geometries, shown in Fig. 10. Separation of the 7075-T6 alloy structure consumed more of the XTA expansion energy, resulting in less outwards bowing of the clevis sides as compared to the 7075-T651 result. The titanium joint result instead showed greater side bowing compared to the aluminums, consistent with less energy consumed until failure for this less ductile material. These observations are in agreement with those made

from basic uniaxial stress-strain-energy responses, suggesting that simple approach is a useful method for design optimization and decision making.

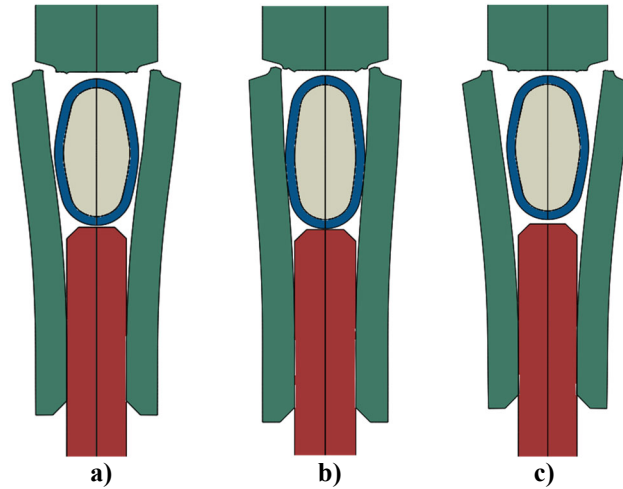


Fig. 10 Post-function deformed states predicted among frangible structural material, a) baseline AA7075-T651, b) AA7075-T6, and c) Ti6Al4V.

Complete fracture sequences predicted for the different joint materials are shown in Fig. 11. Images shown are contoured by damage parameter thereby indicating crack initiation sites during failure progression. Fracture time scales are seen to differ significantly among the various materials studied; 7075-T651 takes about twice as much time to completely separate than Ti6Al4V, and 7075-T6 fractures in about twice as much time as the 7075-T651. These results were therefore organized by key fracture events, corresponding to each row of images, rather than simply by time. This convention was selected in order to focus on differences in fracture development and mechanics. Note that a shorter time to fracture implies a greater margin for severance. Increased margin is a hallmark of more reliable separation systems. Greater margin and potentially improved reliability are thus interpreted for the titanium, as compared to the aluminum alloys considered. While improvements for common geometrical configuration were seen, additional benefits may be possible by considering specifically tailored geometries.

Some additional observations are noted from results in Fig. 11. Just prior to crack initiation and throughout the entire fracture sequence, damage contours are predicted to be nearly identical among aluminum alloys with slightly more localized damage seen with the titanium. Crack initiation location (inside fillet), crack size, orientation ($\sim 45^\circ$), and approximate time of occurrence are predicted nearly identically among all three materials, suggesting initiation is significantly driven by the geometry. Predicted surface profiles at partial fracture reveals the $\sim 45^\circ$ crack orientation is seen to have persisted for all cases but the time scales have started to diverge from one another. By near complete severance, largely flat shaped crack profiles predicted among the 7075-T651 and Ti6Al4V are distinct from the 7075-T6 result which displays a more bilinear profile. This angular profile leads to more rubbing of the crack faces as the side of the clevis bows outwards following severance. Aside from time scales, the overall severance mechanics among materials are in general relatively similar.

The shock output of FJ assemblies characterizes the effective loading transmitted to attached structures. It is a measure of energy distributed out from the device that was not consumed by the severance process. This performance metric is of particular interest from a dynamic environments perspective since many systems and payloads (spacecraft and instruments) may be highly sensitive to these shock loads. The effective shock output was defined here as the net dynamic load transmitted above the separation plane, quantified as the force time history and its time integral, the impulse. These output measures were extracted from the simulations by monitoring the total force acting on a cross-sectional plane just above the FJ clevis member taper. Conceptually, this corresponds to the transmitted load that drives the dynamic environment of attached structures.

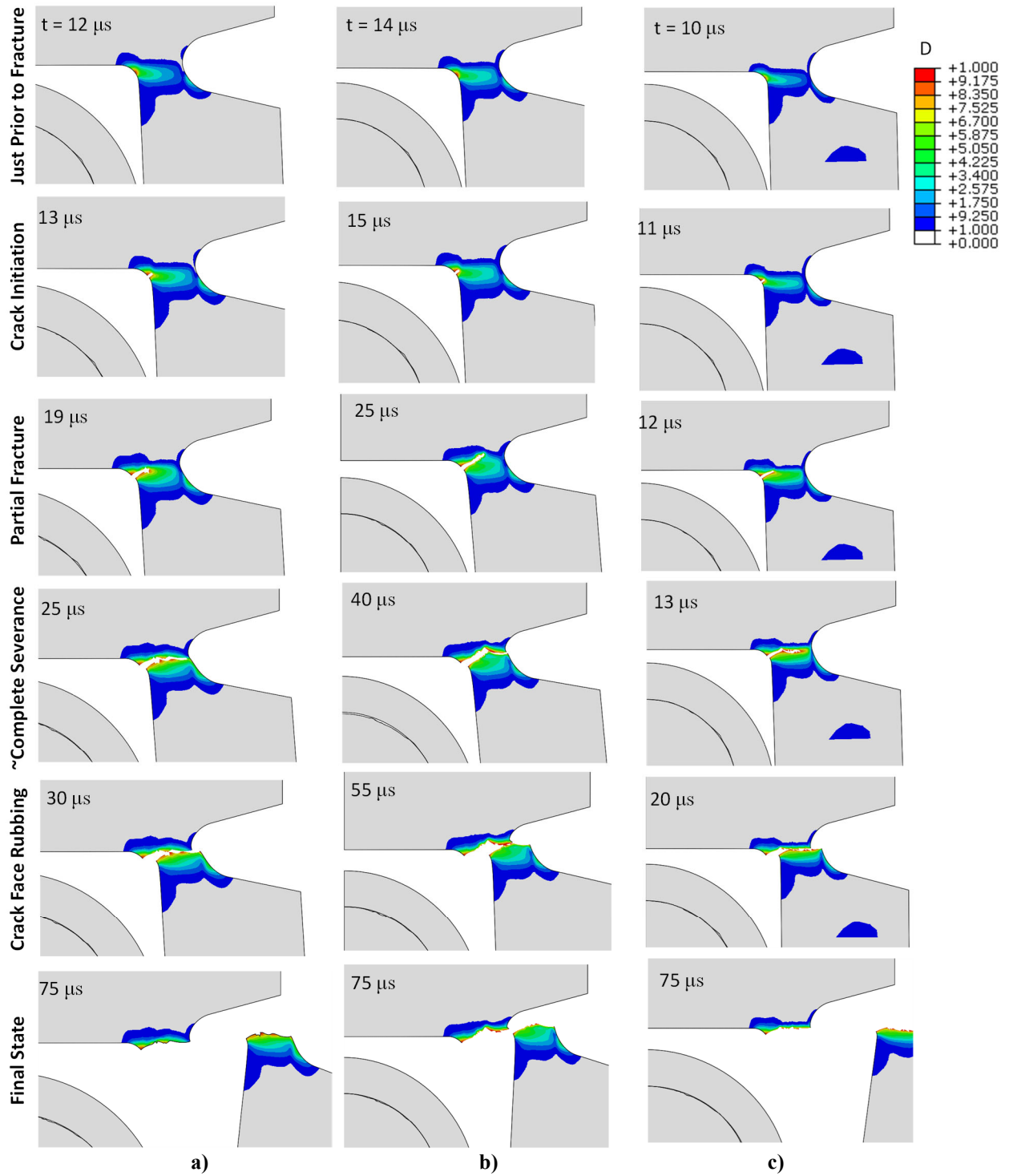


Fig. 11 Fracture sequences predicted as a function of structural material, a) baseline AA6061-T651, b) AA6061-T6, and c) Ti6Al4V.

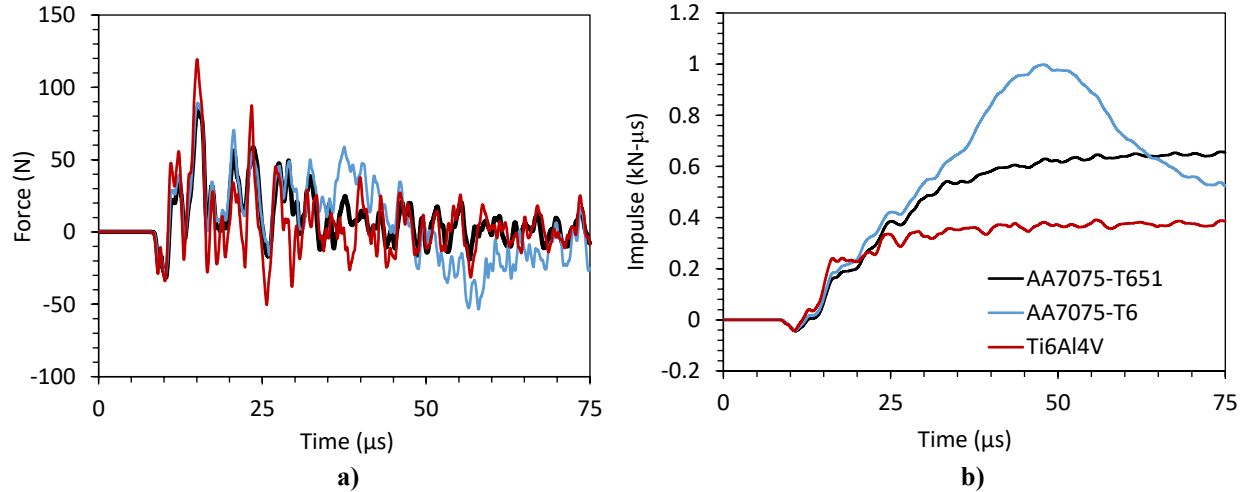


Fig. 12 Effective shock output as a function of frangible structural material, a) force and b) impulse histories.

Effective shock outputs computed from simulation results for the aluminum and titanium alloys are shown in Fig. 12. The particular FJ design studied here is a non-thrust producing variant. Therefore, the net force transmitted is due to stress wave propagation where various wave reverberations lead to the highly oscillatory, ringing nature seen in the force signals of Fig. 12a). The general character of all three force signals is largely similar, as expected given that all originate from the same XTA shock source. Force and impulse signals produced for the aluminum alloys are nearly identical up to $\sim 30 \mu\text{s}$. The titanium displayed higher peak force amplitudes but followed very similar trends and frequency content. Beyond $\sim 30 \mu\text{s}$, the 7075-T651 and Ti6Al4V results trend about a nominal zero mean force level. The 7075-T6 result instead displayed an additional, lower frequency oscillatory character that persisted later in time, causing the apparent decay in impulse seen in Fig. 12b). The titanium is seen to have transmitted the least impulse among the cases studied. Impulse magnitudes were found to be consistent with the time scale of fracture and follow a near-perfect linear trend (coefficient of determination $R^2 = 0.998$). This observation follows directly from the fact that the transmitted loading is terminated once the load path is broken. Notable differences in force and impulse signals among aluminum alloys after $\sim 30 \mu\text{s}$ corresponded to the same time scale where differences in crack mechanics were shown in Fig. 11, again consistent with the load path (or lack thereof) mechanism. An inversely correlated relationship between transmitted impulse and joint side bowing deformation (seen in Fig. 10) was also noted. This relationship is expected from energy consumption arguments.

D. Pyroshock Performance Study

Observations from the fracture performance study are insightful but are not necessarily directly indicative of resulting pyroshock dynamic environments. A common means of experimentally characterizing pyroshock environments in a laboratory setting is by attaching an ordnance device to a simple metallic test plate instrumented with accelerometers. The induced shock environment is then measured from the plate response following activation of the device. This concept was replicated via simulation, as a means to connect FJ device output to the resulting pyroshock environment that may be expected. Such an arrangement is similar to experiments described in Gorfain [14].

A flat 7075 aluminum test plate was assumed to have a linear FJ segment attached along the full length of its bottom edge, as shown in the solid geometry of Fig. 13. This 0.9 m long x 1.2 m tall x 5 mm thick plate was modeled using shell finite elements. The test plate was discretized by a 6 mm mesh size that is sufficient to resolve flexural waves with characteristic frequencies excess of 10 kHz. Activation of the FJ would cause a detonation wave to run along the length of the MDF, producing dynamic fracture of the joint structure that would progress from left to right, in an unzipping fashion as indicated in the top-left image of Fig. 14. Simulation of this scenario was conducted using the technique presented in [14]. Results for the 7075-T651 and Ti6Al4V frangible joints were considered here to probe the hypothesis that the titanium joint may produce a lower shock environment. An array of three locations were monitored to evaluate the predicted pyroshock environment akin to accelerometers in a test. The top-left image of Fig. 14 shows these response locations denoted by A1 – A3, spaced at 0.3 m increments along the height of the plate. Acceleration time histories and corresponding shock response spectra (SRS) were predicted at these locations along the transmission path, examined in each of the axial (Y), lateral (X), and normal (Z) response directions.

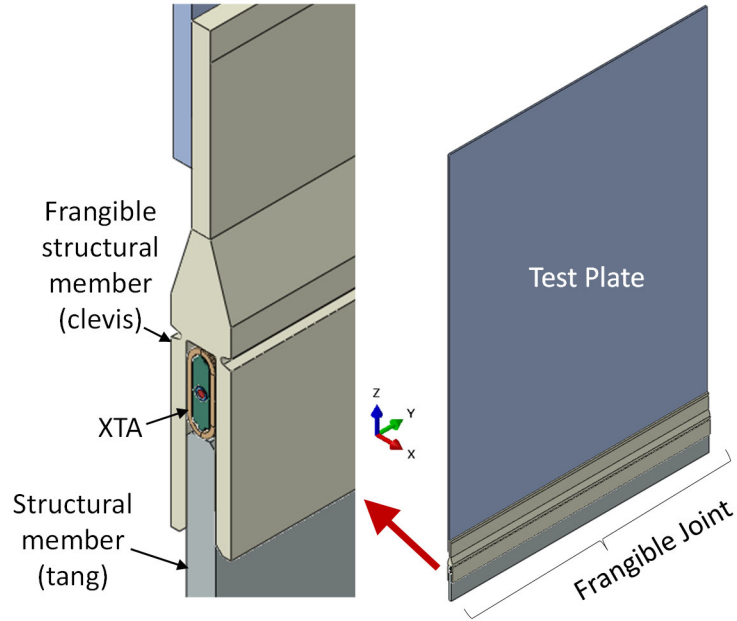


Fig. 13 Solid geometry for pyroshock response arrangement.

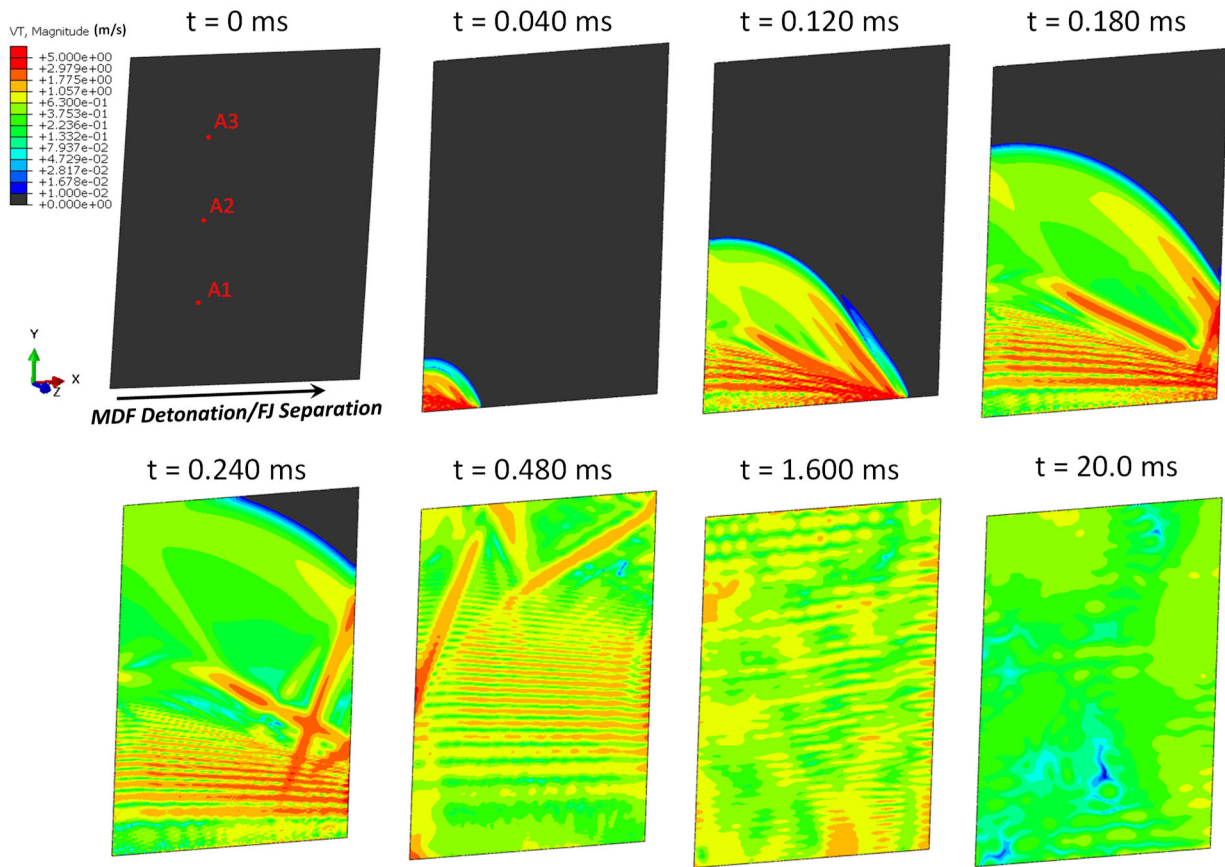


Fig. 14 Predicted sequence of FJ-induced shock propagation on a general flat aluminum plate.

Overall test plate response induced by FJ activation was first examined spatially. Contours of particle velocity throughout the test plate are shown in Fig. 14 for the full 20 ms sequence, spanning FJ initiation, complete separation, and subsequent plate reverberation. The top row of images shows the initial shockwave propagation that occurred early in the sequence while the bottom row of images shows wave-wave and wave-surface interactions that ultimately transition into a reverberant response. Imagery in Fig. 14 corresponds to that for the aluminum FJ, with the velocity field from the titanium FJ being qualitatively very similar and thus not shown. This is expected given that the fundamental nature of wave propagation observed are primarily governed by the test plate characteristics.

The predicted effect of FJ material selection on pyroshock environments are considered in a manner matching typical practices in experiments: by observing acceleration time histories and SRS characterizations of the dynamic environment. Note that simulation results were acquired, and signal processed following typical best practices used in making pyroshock test measurements [14]. Acceleration signals predicted for normal response directions at each location are shown Fig. 15, with the aluminum and titanium FJ results in the top and bottom plots, respectively. Though signal structure and trends along the transmission path are similar among the two cases, significantly lower acceleration amplitudes were predicted for the titanium FJ case. This observation is consistent with the shorter timescale for separation and lower impulse delivered during device function, despite that higher peak forces were predicted in that case.

Further comparison of pyroshock environments predicted among FJ material selections are made on the basis of maxi-max acceleration SRS profiles, computed in $1/8^{\text{th}}$ octave bands over the typical 100 Hz – 10 kHz bandwidth of interest with resonance amplification factor $Q = 10$. Plate normal, axial, and lateral SRS curves are shown in Fig. 16. Results from the aluminum FJ are plotted as solid curves while titanium FJ results are shown as dashed curves. In all locations and response directions, SRS for the titanium FJ is seen to lie below that for aluminum FJ, across the full bandwidth. Narrow frequency band SRS features among all response directions and locations are identical among FJ materials, they simply display uniform differences in level broadband. These observations are consistent with the fact much of the SRS shape is attributed to characteristics of the test plate, while the overall SRS level is fundamental to the shock excitation, which in this case is the source FJ device. The apparent reduction in pyroshock environment predicted for the titanium is quantified on the basis of SRS attenuation expressed in dB, relative to that from the baseline aluminum FJ results. Plots of SRS attenuation for all locations and response directions are presented in Fig. 17. Broadband attenuation of at least -3.8 dB was predicted, with as much as -5.3 dB predicted narrow band. These results do support the hypothesis that a FJ constructed from Ti6Al4V structural materials may enable significant reduction in induced pyroshock environments.

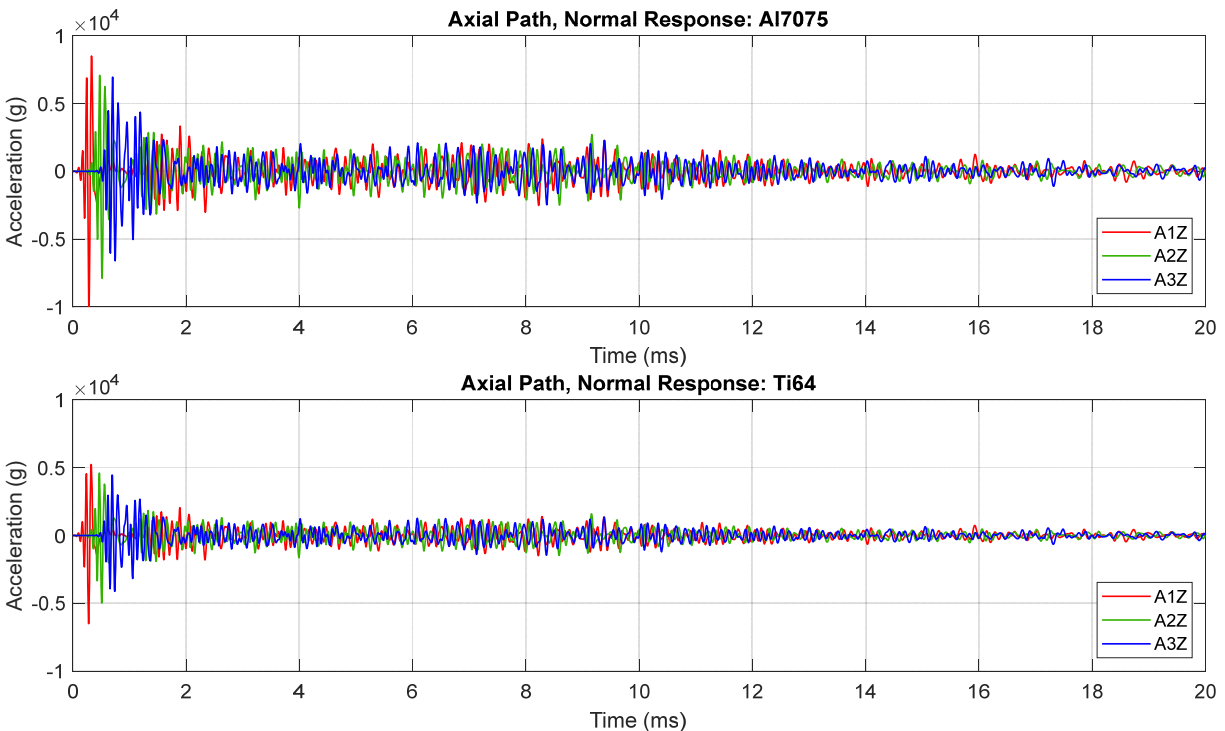


Fig. 15 Acceleration histories predicted for shock transmitted by aluminum and titanium frangible joints.

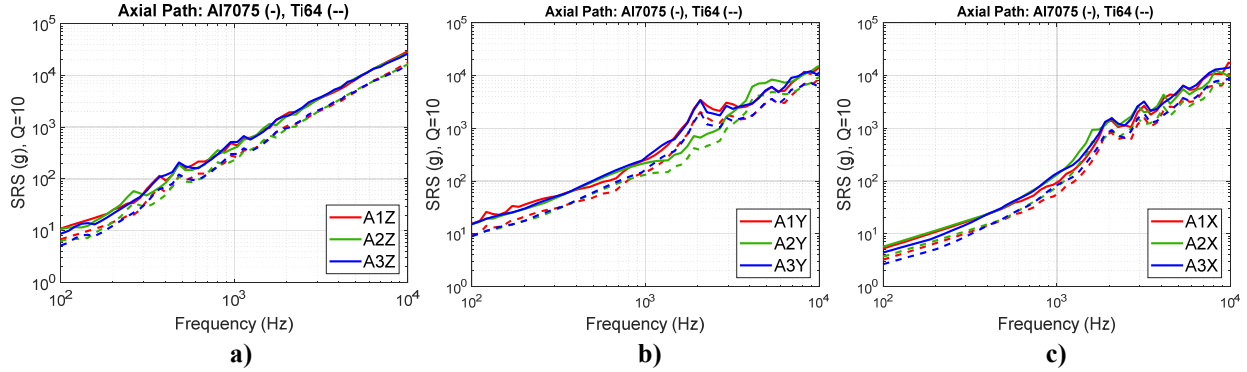


Fig. 16 Predicted SRS environments for aluminum (solid) and titanium (dashed) frangible joints, a) normal response, b) axial response, and c) lateral response.

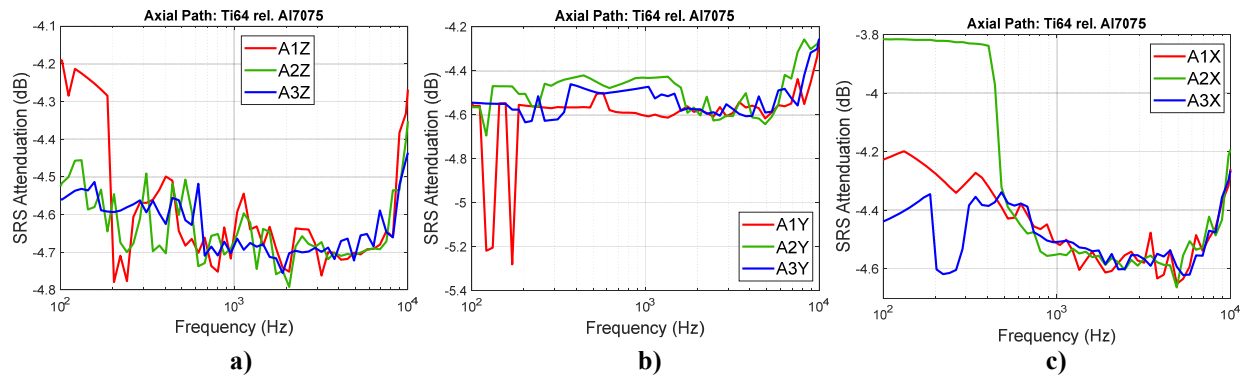


Fig. 17 Predicted SRS attenuation for titanium frangible joint relative to an aluminum baseline, a) normal response, b) axial response, and c) lateral response.

III. Conclusion

Detailed analysis of frangible joint performance was studied using nonlinear, explicit dynamics finite element simulations. Confidence in the modelling of key aspects of functional behavior with this ordnance device, namely dynamic fracture driven by explosive-induced loading, was gained through comparison to various experimental data sources in the open literature. Modeling was used to gain insights into the dominant mechanisms governing successful performance of this complex separation system. A tensile initiated, shear dominated ductile fracture propagation mechanism was predicted with this device design.

Sensitivities of frangible structural material selection on structural severance behavior and shock output were studied at several levels using the model developed. The basic frangible joint design was seen to be quite robust as successful severance was predicted for all three metallic materials examined. The time scale of fracture and transmitted shock output were found to be key parameters, directly related to the characteristic energy required to fracture the structural member. These metrics suggested opportunities to potentially increase separation margin and lower transmitted shock output. Device performance was specifically considered for the case where a titanium alloy used in place of the aluminum typically employed, virtually testing the suggested design-performance hypothesis. With knowledge of associated FJ device shock output, the effects on induced pyroshock dynamic environments were directly explored. Subsequent pyroshock simulations showed trends consistent with the underlying device performance analyses: 1) a titanium FJ may be expected to produce a significantly reduced shock environment relative to an aluminum design, and 2) shorter severance timescales appeared to be positively correlated with lower induced pyroshock levels. These findings provide interesting insights that may enable frangible joint designs providing better functional performance.

The direct connection made between separation device physics and resulting pyroshock environment produced was a notable outcome, as are some simple guidelines offered to inform improved designs. Although simulation results were compelling, experimental confirmation of these findings are needed to demonstrate that predicted results hold true. Consideration of all requirements relevant to flight systems would also be necessary to determine if a frangible

joint made of titanium, is a feasible option. Future work will seek to address both issues and continue to explore innovations in ordnance devices and pyroshock design practices.

References

- [1] Malik, T., Weitering, H., Wall, M., Bartels, M., Gohd, C., and Pultarova, T., "NASA Pinpoints Causes for Climate Satellite Crash," *Space.com*, 17 July 2009, URL: <https://www.space.com/6998-nasa-pinpoints-climate-satellite-crash.html> [retrieved 16 June 2017].
- [2] Svitak, A., and Moring Jr., F., "NASA Launched Glory Despite Open Component Questions," *Aviation Week and Space Technology*, 17 December 2012, URL: <http://aviationweek.com/awin/nasa-launched-glory-despite-open-component-questions> [retrieved 16 June 2017].
- [3] Sheetz, M., "Northrop Grumman, Not SpaceX, Reported to be at Fault for Loss of Top-Secret Zuma Satellite," *CNBC*, 9 April 2018, URL: <https://www.cnn.com/2018/04/09/northrop-grumman-reportedly-at-fault-for-loss-of-zuma-satellite.html> [retrieved 12 June 2018].
- [4] Duprey, K. E., and Keon, S. P., "Analysis and Development of a Low Temperature Frangible Joint Assembly," 42nd AIAA/ASME/SAE/ASEE Joint Propulsion Conference & Exhibit, AIAA Paper 2006-4986, July 2006.
- [5] Alcantara I., "Quasi-Static Fracture Toughness Testing of 7075 Aluminum for Spacecraft Separation Joint Applications," M.S. Thesis, Department of Metallurgical, Materials, and Biomedical Engineering, The University of Texas at El Paso, El Paso, TX, 2017.
- [6] Choi, M., Lee, J.-R., and Kong, C.-W., "Development of a Numerical Model for an Expanding Tube with Linear Explosive Using AUTODYN," *Shock and Vibration*, Vol. 2014, Article 436156, March 2014.
- [7] Chambers N. R., "Design and Numerical Simulation of a Linear Shaped Charge Separation Mechanism for First Stage Separation of the Ares I Launch Vehicle," M.S. Thesis, Department of Aerospace Engineering, Mississippi State University, Mississippi State, MS, 2009.
- [8] Goldstein S., Wong, T. E., Frost, S. W., Gageby, J. V., and Pan, R. B., "Bolt Cutter Functional Evaluation," 2nd NASA/DOD/DOE Pyrotechnic Workshop, pp. 243-267, February 1994.
- [9] Wang, X., Qin, Z., Ding, J., and Chu, F., "Finite Element Modeling and Pyroshock Response Analysis of Separation Nuts," *Aerospace Science and Technology*, Vol. 68, pp. 380-390, May 2017.
- [10] Duprey, K. E. and Saucier, E. R., "Separation Systems Comparison for ARES I Launch Vehicle," 44th AIAA/ASME/SAE/ASEE Joint Propulsion Conference & Exhibit, AIAA Paper 2008-4514, July 2008.
- [11] Ott, R. J. and Folman, S., "Full-Scale Pyroshock Separation Test: Attenuation with Distance," *Journal of Spacecraft and Rockets*, Vol. 54, Issue 3, pp. 602-608, March 2017.
- [12] McLeod, L. and Tatum, S., "Modeling of Ordnance-Induced Pyrotechnic Shock Testing," *Proceedings of the 83rd Shock and Vibration Symposium*, U-51, Shock and Vibration Exchange, New Orleans, LA, 2012.
- [13] Dassault Systems Simulia Corp., 2022. The Abaqus finite element code.
- [14] Gorfain, J. E., "Evaluation of Line Source-Induced Shock Environments," *Proceedings of the 31st Aerospace Testing Seminar*, The Aerospace Corporation, Los Angeles, CA, October 2018.
- [15] Stockinger, J., Shen, F., Bowers, G., Pan, M., and Whalley, I., "Delta IV Evolved Expendable Launch Vehicle Ordnance Overview," 41st AIAA/ASME/SAE/ASEE Joint Propulsion Conference & Exhibit, AIAA Paper 2005-3655, July 2005.
- [16] Fritz, J. E., "Separation Joint Technology," 39th AIAA/ASME/SAE/ASEE Joint Propulsion Conference, AIAA Paper 2003-4436, July 2003.
- [17] Johnson, G. R., and Cook, W. H., "A Constitutive Model and Data for Metals Subjected to Large Strains, High Strain Rates, and High Temperatures," *Proceedings of the 7th International Symposium on Ballistics*, Hague, Netherlands, 1983, pp. 541-548.
- [18] Johnson, G. R., and Cook, W. H., "Fracture Characteristics of Three Metals Subjected to Various Strains, Strain Rates, Temperatures and Pressures," *Journal of Engineering Fracture Mechanics*, Vol. 21, No. 1, pp. 31-48, 1985.
- [19] Corona, E. and Orient, G. E., "An Evaluation of the Johnson-Cook Model to Simulation Puncture of 7075 Aluminum Plates," SAND2014-1550, 2014.
- [20] Kay, G., "Failure Modeling of Titanium-61-4V and 2024-T3 Aluminum with the Johnson-Cook Material Model," LLNL UCRL-ID-149880, 2002.
- [21] Senthil, K., Iqbal, M. A., Chandel, P.S., and Gupta, N. K., "Study of the Constitutive Behavior of 7075-T651 Aluminum Alloy," *International Journal of Impact Engineering*, Vol. 108, 2017, pp. 171-190.
- [22] Brar, N. S., Joshi, V. S., and Harris, B. W., "Constitutive Model Constant for Al7075-T651 and Al7075-T6," *AIP Conference Proceedings* 1195, 2009. pp. 945-948.
- [23] Steinberg, D. J., "Equation of State and Strength Properties of Selected Materials," LLNL UCRL-MA-106439 Change 1, 1996.
- [24] Rice, R. C., Jackson, J. L., Bakuckas, J., and Thompson, S., "Metallic Materials Properties Development and Standardization," DOT/FAA/AR-MMPDS-01, 2003.
- [25] Bement, L. J., and Schimmel, M. L., "A Manual for Pyrotechnic Design, Development and Qualification," NASA TM-110172, 1995.
- [26] Lee, E. L., Walton, J. R., and Kramer, P. E., "Equation of State for the Detonation Products of Hexanitrostilbene at Various Charge Densities," LLNL UCID-17134, 1976.

- [27] Lesuer, D. R., Kay, G. J., and LeBlanc, M. M., "Modeling Large Strain, High Rate Deformation in Metals," *Proceedings of the 3rd Biennial Tri-Laboratory Engineering Conference, on Modeling and Simulation*, Pleasanton, CA, 1999.
- [28] Millet, J. C. F., Whiteman, G., Stirk, S. M., and Bourne, N. K., "The Shock Induced Shear Strength in a Silastomer," *Proceedings of the SEM Annual Conference*, Albuquerque, New Mexico, June 2009.
- [29] Coe, J. D., "SESAME Equations of State for Stress Cushion and Related Materials," LANL LA-UR-15-21390, 2015.
- [30] Maurel-Pantel, A., Fontaine, M., Thibaud, S., and Gelin, J. C., "3D FEM Simulations of Shoulder Milling Operations on a 304L Stainless Steel," *Simulation Modelling Practice and Theory*, Vol. 22, 2012, pp. 13-27.